Anomalous ionic transport in tunable angstrom-size water films on silica

Aymeric Allemand, Menghua Zhao, Olivier Vincent, Remy Fulcrand, Laurent Joly, Christophe Ybert, Anne-Laure Biance

Anomalous ionic transport in tunable angstrom-size water films on silica

Aymeric Allemand[a], Menghua Zhao[a,1], Olivier Vincent[a], Remy Fulcrand[a], Laurent Joly[a], Christophe Ybert[a], and Anne-Laure Biance[a,1]

[a]Univ Lyon, Univ Claude Bernard Lyon 1, CNRS, Institut Lumière Matière, F-69622, VILLEURBANNE, France

This manuscript was compiled on November 1, 2023

Liquid and ionic transport through nanometric structures is central to many phenomena, ranging from cellular exchanges to water resource management or green energy conversion. While pushing down towards molecular scales progressively unveils novel transport behaviors, reaching ultimate confinement in controlled systems remains challenging and has often involved 2D Van der Waals materials. Here, we propose an alternative route, which circumvents demanding nanofabrication steps, partially releases material constraints, and offers continuously tunable molecular confinement. This soft-matter-inspired approach is based on the spontaneous formation of a molecularly thin liquid film onto fully wettable substrates in contact with the vapor phase of the liquid. Using silicon dioxide substrates, water films ranging from angstrom to nanometric thicknesses are formed in this manner, and ionic transport within the film can then be measured. Performing conductance measurements as a function of confinement in these ultimate regimes reveals a one-molecule thick layer of fully hindered transport nearby the silica, above which continuum, bulk-like approaches account for experimental results. Overall, this work paves the way for future investigations of molecular scale nanofluidics and provides novel insights into ionic transport nearby high surface energy materials such as natural rocks and clays, building concretes, or nanoscale silica membranes used for separation and filtering.

Nanofluidics | Ionic transport | Water film

Transport of liquids and ions at the nanoscale, referred to as nanofluidics, has attracted tremendous attention for its wide applications in desalination and filtration (1), clean energy extraction (2), design of new concepts of fluidic semiconductors (3) and biomolecular diagnosis (4). From a fundamental point of view, nanofluidics plays a key role in many fields of science, from the nanoscale communication mechanisms involved in cell biology (5) to macroscopic geological systems, involving for example transport of water and ions in soils, natural rocks, and clays. Conventional continuum descriptions have been challenged for ions and liquid transport in sub-nanometric slits or tubes (6), with original phenomena arising from confinement such as anomalous ion mobility (7, 8), ultra-fast flows in nanotubes (9, 10) or giant osmotic energy conversion (11).

One particular property of the nanoscale is a diverging surface-to-bulk ratio. Complex behaviors have often been attributed to enhanced surface effects. The most classical one concerns ionic conductivity, as its value is critical to determine the yield of energy conversion processes in nanofluidic membranes (11, 12). The ionic conductivity of a channel has generally at least two contributions; one originates from the bulk and is directly linked to the number of charge carriers that have been added in the solution (such as a fixed salt concentration or pH), and the other originates from surface charges (for example from the ionization of the surface and the release of counter-ions, among other possible mechanisms). Experiments at low salt concentrations give access to the surface conductivity contribution. Indeed, a plateau of the conductance of the channel as a function of salt concentration (11, 13, 14) is observed provided that the so-called Dukhin number, $\mathrm{Du} = |\sigma|/ehc$ (with σ the surface charge density on the channel walls, c the bulk salt concentration, e the elementary charge, and h the channel thickness), that compares the number of surface and bulk charge carriers, is larger than one. Deviations from this simple picture have been observed experimentally, for transport in carbon or boron nitride nanotubes (11, 14, 15), hydrophobic nanopores (16), graphene nanoslits (7) or proteinic channels (17).

On the one hand, continuous descriptions suggest that these deviations can be due to complex charge dissociation mechanisms at the interface (18), hydrodynamic slip and charge mobility along the interface (7, 19), or a subtle interplay between electronic properties of the material and ionic transport at the interface (6). In any cases, such surface mediated mechanisms involve molecular scale static or dynamical properties (20, 21).

On the other hand, these deviations can also originate from ultimate molecular confinement, resulting in the failure of the macroscopic continuum constitutive laws. For example, basic

Significance Statement

Nanoscale transport of ions and liquids is crucial for many geological and biological processes, but also for the design of efficient membranes for desalination, filtration, or osmotic energy harvesting. While the most salient behaviors arise at the molecular scale, such ultimate confinement has so far been achieved on a limited number of geometrical designs restricted to specific materials. To bypass previous technological limitations, we investigated transport in molecular-thick water films that spontaneously form onto fully wettable substrates surrounded by water vapor. We observed that ion transport is hindered nearby silica within a molecular layer of ~ 3 Å, above which continuum models successfully capture our observations. Our approach opens up a new route to explore ultimate nanofluidic transport on various surfaces.

A.-L.B., C.Y., and L.J. designed research, A.-L.B., C.Y., O.V., M.Z. and A.A. designed the experiments, A.A. and M.Z. performed the experiments and analyzed the data, A.-L.B., C.Y., L.J., and A.A. derived the model, R.F. carried out electrode deposition, A.-L.B., C.Y., L.J., O.V., A.A. and M.Z. wrote the paper.

The authors declare no competing interest.

[1]To whom correspondence should be addressed. E-mail: menghua.zhao@univ-lyon1.fr, anne-laure.biance@univ-lyon1.fr

physical constants known for the bulk are challenged, such as the dielectric constant of water (22), reported to drastically decrease from 80 to 2 for a 1 nm-confined water film in a graphene slit; similarly, viscosity can strongly increase for aqueous electrolyte of thickness below 3 nm (23, 24).

To test these ultimate regimes, experimental systems have been developed, including nanopores (25), 1D nanotubes (11, 14, 15), or 2D nanoslits (7, 8, 26), and rich physical phenomena have been revealed. But up-to-date investigations are still restricted to very specific systems, such as carbon-based channels (graphene (27), graphite (28, 29)), and similar van der Waals material systems (hBN (22), MoS_2 (25)), and with geometrical confinement down to one monolayer of graphene (6, 28, 30). Despite showing remarkable and promising behaviors, these systems constitute a very specific class of materials, which consists of layered smooth individual atomic planes. Some extensive studies reported transport properties across proteinic nanopores (31), but restricting the analysis to the complex nature of the biological nanopores. On the contrary, studies in the vicinity of oxide substrates are limited to larger scales (13, 32, 33), with minimum confinement to 2 nm so far. In sharp contrast to the loose molecular interactions on carbon-based or van der Waals materials, silicon dioxide is hydrophilic, with strong adhesion to adjacent water molecules (34–36). One may wonder how liquids and ions are transported in such a strong liquid/solid interacting channel with a size comparable to a few molecules, and if additional effects need to be addressed. Moreover, most existing fine-thickness-controlled nanochannels are too delicate to fabricate and leakage/blockage may pose a strong issue for practical applications (28). A cheap, yet easy-to-fabricate nanoscale channel is needed.

To tackle the above-mentioned questions, we have developed an experiment that takes advantage of surface wettability of silicon dioxide, which allows us to deposit a thin water layer, whose thickness can be continuously tuned from 0.3 to 2 nm. To achieve this, our device with a silicon dioxide interface was placed in a vacuum chamber with controlled humidity, which resulted in predictable water condensation on the silica surface. In this situation, the water film is free of contamination from the surroundings, in sharp contrast to most other nanofluidic devices (6, 30) where liquid reservoirs are connected to air. We then detected the conductance within this ultra-clean liquid film by applying an external electric field, and further deduced the magnitude of ion transport in the liquid. We discovered a non-linear response of conductance as a function of film thickness. A modified PNP (Poisson-Nernst-Planck) theory based on continuum mechanics successfully captures our observations, when taking into account that the transport of a monolayer of ions adjacent to the wall is totally hindered.

This result contrasts with the singular mobility reported for 2D materials, stressing out the critical impact of the nature of the substrate on nanofluidic ionic transport.

Experiments and results

Tunable angstrom-size water films for nanofluidics. To date, ultimate molecular confinement has been reached either in biological pores (31) or through advanced nanofabrication strategies (8). In the spirit of previous proposals for obtaining confinements of tens to hundreds of nanometers (37, 38), we extend soft-matter approaches to nanofluidics towards the building of molecular-thick liquid films. Indeed a liquid film spontaneously assembles onto fully-wettable surfaces when exposed to its vapor (34, 35). Such a condition can be met with a clean silica surface under water vapor atmosphere, the pressure of which can be used to continuously tune the liquid film thickness in the angstrom to nanometer range (39–42).

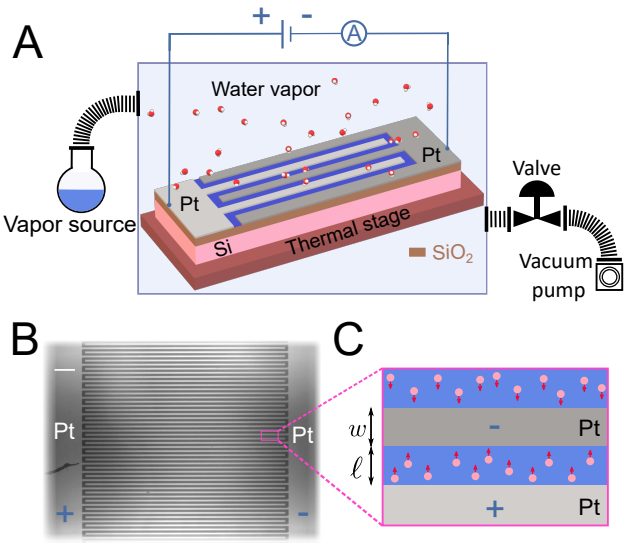

Fig. 1. Scheme of the experimental setup and picture of the substrate. (A) The substrate is placed in a vacuum chamber that eliminates airborne contaminants and oxidization. Water vapor with controlled pressure, set by the vapor source temperature T_b, flows into the chamber and is adsorbed onto the silicon dioxide surface between the electrode pads, forming a thin liquid film. The silicon dioxide temperature T is tuned by the underlying thermal stage, which determines the saturation vapor pressure of the electrode, and changes the thin film thickness. A sinusoidal voltage bias is applied to the liquid film and the current response is recorded to estimate its conductance. (B) Microscopic view of the sample under reflection light. Scale bar: 1 mm. The gray-shined part on the sample corresponds to the platinum electrode and the dark-shaded part corresponds to the SiO_2 surface between the electrodes. The interlaced design of the platinum deposition amplifies the electrode total length to 1.49 m. (C) Zoom-in of the patch framed in (B). Protons (pink circles) migrate (red arrows) between the two electrodes. Both the gap, ℓ, between two platinum branches and the width, w, of each platinum branch are 100 µm.

In practice, we use substrates that consist of SiO_2 layers grown on silicon wafers. The surface was characterized by AFM and found to be smooth at the atomic scale (43), with a rms roughness of ≈ 0.2 nm and absolute value of the average of profile height deviations from the mean line $R_a \approx 0.17$ nm (see material and methods for details). This silica substrate is treated by oxygen plasma prior to the experiment and then introduced in a low-pressure experimental chamber where its temperature T can be controlled (Fig. 1A). The chamber is put under vacuum conditions and then connected to a water vapor source dipped in a regulated thermal bath at a fixed temperature T_b, so that the relative humidity (RH) in contact with the substrate can be finely controlled with the substrate's temperature T. Low-pressure conditions help to maintain the physio-chemical properties of the silicon dioxide surface, for example by removing airborne contamination and oxidization.

The thickness of the liquid film is measured by a spectroscopic ellipsometer that is adapted to our vacuum chamber (Fig. 2A). The measurement of the attenuation and polarization of the reflected light signal on the sample gives access to the water film thickness h, considering an optical model with three material layers (silicon at the bottom, thin silica

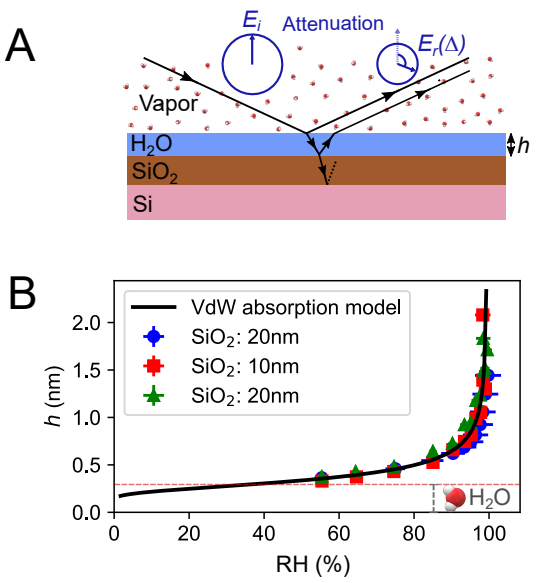

Fig. 2. Ellipsometric measurements of liquid film thickness. (A) Principle of ellipsometry measurements. (B) Thickness of the water film as a function of relative humidity in the chamber on three SiO_2 surfaces: 20 nm-thick (blue circles), 10 nm-thick (red squares) and 20 nm-thick (green triangles). Black solid line corresponds to the van der Waals adsorption model. Best fit gives the Hamaker constant $A_{slv} = (-6.79 \pm 0.07) \times 10^{-20}$ J.

layer, adsorbed water layer at the top). In situ experiments performed on SiO_2–Si sample under vacuum (no water) give access to the reference parameter for silicon and silica for the interpretation of ellipsometry data. An additional water layer is then incorporated into the model structure (Fig. 2A) and the water film thickness h is then estimated with an accuracy of 0.3 nm. As expected, h increases with RH, to diverge at RH=100% (Fig. 2B). Optical monitoring of the surface was carried on to ensure that no signature of microscopic droplets or dry patches could be detected, as expected for a fully-wettable substrate. Considering the surface roughness and this observation, the liquid film is assumed to be homogeneous. However, droplets or patches below the microscopy resolution, 1 µm, can not be detected due to the optical limitations of the set-up.

Quantitatively, balancing the water chemical potential in the vapor and in the film allows us to write down the h(RH) relation in terms of the disjoining pressure (44), $\pi(h) = -\rho_l k_B T \ln(\text{RH})$, with ρ_l the liquid density, k_B the Boltzmann constant and T the temperature. For Van der Waals (VdW) interactions, the disjoining pressure classically reads $\pi(h) = -A_{slv}/(6\pi h^3)$ with A_{slv} the solid-liquid-gas Hamaker constant, which quantifies interaction energy between water vapor and solid through the water film. In principle other interactions may contribute to the disjoining pressure atop the VdW ones, such as electrostatics or specific surface adsorption (34, 44). In the present situation, however, VdW contribution turns out to be dominant as evidenced by the scaling law $\pi(h) \propto h^{-3}$ exhibited by experimental measurements (see SI appendix). Best fit to experimental data yields in $A_{slv} = -(6.79 \pm 0.07) \times 10^{-20}$ J, in good agreement with computed values (45). Note that substrates with various SiO_2 layer thicknesses show similar quantitative results (Fig. 2B), thus evidencing negligible effect from the silicon base.

Probing Conductance. The conductance of the condensed film is measured by using platinum electrodes deposited on the silicon dioxide surface (Fig. 1A). The two facing electrodes are fabricated in an interlaced comb-shaped design (Fig. 1B) to increase the electrode total length and thus the signal magnitude.

A sinusoidal electrical voltage (1 V, 10 Hz) is applied between the two platinum electrodes, and the corresponding current circulating across the liquid film between the electrodes (Fig. 1C) is detected by a homemade amplifier. AC actuation avoids ion accumulation and depletion near the electrodes, and maintaining the signal amplitude below 1 V prevents water hydrolysis (redox potential of water is 1.23 V). A typical measurement of the imposed voltage and the induced current is reported in Fig. 3B, for a humidity of RH = 99.1 %. From an analysis of the amplitude of the signal and the phase shift, taking into account the system leakage thoroughly characterized under vacuum conditions (see SI appendix for details), we extract the film properties and in particular the conductance in the liquid, denoted G and reported in Fig. 3C.

By continuously varying RH, the nanometric film conductance, G, as a function of film thickness is summarized in Figures 3(C). We report two different experiments performed at two vapor source temperatures, $T_b = 6.01 \pm 0.02$ °C shown by the green data set (case I) and $T_b = 15.81 \pm 0.03$ °C shown by the blue data set (case II). In both cases, we performed loading measurements of G associated with gradual increase of RH (open symbols in Fig. 3C), and unloading measurements upon RH decrease (solid symbols in Fig. 3C). Overall, data show amplitude variability between samples but also a hysteretic behavior for G, which is smaller upon loading than upon unloading.

Such a hysteresis is reminiscent of water uptake hysteresis observed in porous materials during humidity cycles (46). Note however that in the present system, the liquid film itself does not display any hysteretic behavior with a thickness independent of the loading or unloading cycle. A possible origin for back-and-forth differences in conductance values could be attributed to the film–electrode connection, which involves water menisci. Indeed contact line pinning is a well-known and unavoidable source of hysteresis that will change the geometry of the connection with the water film depending on water uptake or release.

Now concentrating on the generic features displayed by these measurements, we evidence that the film conductance G non-linearly increases with the film thickness h. At small thicknesses comparable to the size of a single water molecule ($h \leq 0.3$ nm), G is undetectable, suggesting a significant hindering of proton mobility at this length scale (see hereafter for a detailed discussion). The conductance then increases, before reaching a plateau at moderate thicknesses $h \simeq 1.2$ nm. Interestingly, this plateau is reminiscent of the so-called surface conductance regime evidenced upon confinement, when the thickness h becomes smaller than the so-called Dukhin length (6, 11, 13, 33). In fact, below such a confinement scale, the concentration of ionic species in the channel becomes dominated by the number of counter-ions needed to balance the surface charge. If this surface charge is constant, this yields a fixed conductance independent of further confinement or bulk electrolyte concentration. A more adequate description

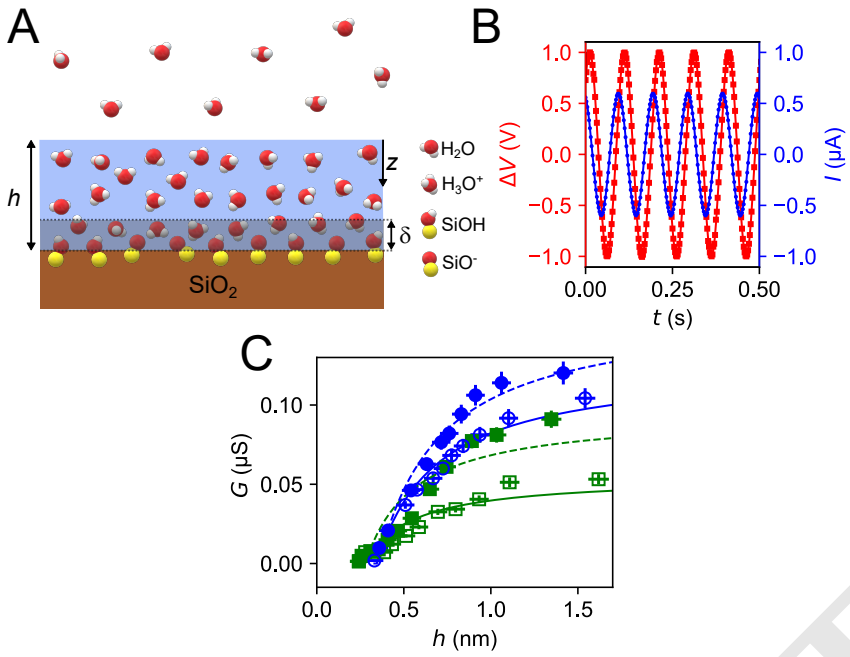

Fig. 3. Conductance measurements in a liquid film. (A) Schematic of the hindered diffusion layer model. The z direction is perpendicular to the external electric field, with $z = 0$ being the liquid-vapor interface and $z = h$ the liquid-solid interface. A hindered layer of thickness δ is represented next to the solid. (B) Typical voltage input (red) and raw current response (blue) of our experimental system. The input voltage is a 1 V AC sine wave with a frequency of 10 Hz. Scattered points correspond to experimental data and fitting curves are shown as lines. (C) Liquid film conductance, G, as a function of water film thickness h. Scattered points represent experimental data with open and full symbols for a loading and unloading cycle, respectively. Solid and dashed lines show model predictions for a loading (increase of the humidity) and unloading (decrease of the humidity) cycle, respectively. Green and blue colors indicate a vapor source temperature of T_b=6.01 ± 0.02°C (case I) and T_b=15.81 ± 0.03°C (case II), respectively.

is rather to consider that the ionization rate at the surface depends on the film thickness, thanks to a so-called charge regulation mechanism. However, that both the schematic constant charge and the charge regulation pictures may break down in ultimate confinement, with a progressive fading away of the conductance at a finite thickness is a novel feature that we discuss in the following.

Conductance model

Continuum approach. In order to rationalize the above measurements, we now discuss the theoretical modeling of the ionic conductance in our system. As the liquid film comes from water vapor condensation in a vacuum, ions in the water film result from water self-dissociation or ionization of silanol surface groups through: $\mathrm{SiOH} \rightleftharpoons \mathrm{SiO^-} + \mathrm{H^+}$. At pH= 7 and for typical silica surface charges (13, 33, 47), ions concentration is entirely dominated by protons $\mathrm{H^+}$ from the surface reaction (44). In the following, we will therefore neglect water dissociation reaction together with the presence of hydroxide ions $\mathrm{OH^-}$.

Next, we describe the electrostatic potential ψ and ions distribution c_+ in the film by adopting a continuous mean-field Poisson-Boltzmann (PB) equation, in the Gouy-Chapman regime (48, 49) for monovalent ions. We complement this equation by the boundary conditions along the direction z perpendicular to the surface (Fig. 3A). At the free surface $z = 0$, we assume no surface charge and sets the potential to zero so that $\phi'(z = 0) = \phi(z = 0) = 0$, with the dimensionless potential $\phi = e\psi/(k_BT)$. At the silica/water interface, the potential relates to the surface charge density σ according to $\phi'(z = h) = 4\pi\ell_B\sigma/e$ with $\ell_B = e^2/(4\pi\epsilon k_BT)$ being the Bjerrum length that compares Coulombic interactions with thermal energy (see SI appendix for details). Overall, this provides the z profiles for ϕ and c_+ as a function of the film thickness and of the yet-to-be-determined surface charge σ (see SI for complete derivation).

Finally, the water film conductance is obtained according to

$$G = \frac{I}{\Delta V} = \frac{1}{\Delta V} \iint_{\mathcal{S}} \mathbf{j_e} \cdot \mathrm{d}\mathbf{S} \qquad [1]$$

with ΔV the applied voltage between the two platinum electrodes, $\mathcal{S}$ the cross section of the integration domain (here $\mathcal{S} = h \times L$ with L the total length of the electrode), $\mathbf{j_e}$ the current density vector, $\mathbf{j_e} = ec_+(z)\mathbf{v}(z)$, with $\mathbf{v}$ the velocity of ions. The velocity of ions has in principle two contributions (21, 50): one originating from their electrophoretic mobility, and the other one from the electro-osmotic flow generated at the interface. In practice, the electro-osmotic contribution is negligible when the channel size is smaller than the Debye length for a low surface charge density (51–53), and only the electrophoretic effect will be considered in the following (see SI appendix).

To close the description, we need to come back on the surface charge σ and specify its properties. A full description would be to consider that the surface charge is fixed by an ionization ratio that results from a chemical dissociation mechanism (44), i.e., charge regulation mechanism. This is detailed in the discussion section and in the SI appendix, and results in the same quantitative description. However, as a first approach, we will simply consider that the ionization ratio of silanol groups is fixed, independent in particular of the film thickness, thus resulting in a constant surface charge. Accordingly, an equivalent number of charge carriers $\mathrm{H^+}$ is released in the liquid, which can move under an electric field. If the mobility μ_+ of these ions is homogeneous across the water film (a second hypothesis), liquid film conductance will be a constant $G \propto e\mu_+|\sigma|$, referred to as surface conductance regime (11, 13, 21). This behavior is indeed consistent with what is recovered in our experiments for films thicker than 1.2 nm. Nevertheless, it fails to account for the evolution of G down to molecular confinement, where the conductance eventually vanishes.

As is clear from the above discussion, within the present

Table 1. Fitting parameters for the hindered diffusion layer model at constant surface charge density σ

	Loading	Unloading
T_b (°C)	σ (µC m^{-2}), δ (Å)	σ (µC m^{-2}), δ (Å)
6.01 ± 0.02	$-9.50 \pm 0.79, 2.74 \pm 0.19$	$-16.4 \pm 1.6, 2.78 \pm 0.20$
15.81 ± 0.03	$-22.6 \pm 0.8, 3.45 \pm 0.12$	$-28.9 \pm 1.0, 3.55 \pm 0.11$

continuum framework, conductance calculations are based on two assumptions on the surface charge and on the ions dynamics. As mentioned above, it is possible to relax the constant surface charge assumption, using a more adequate charge regulation mechanism (44). This approach is however not capable alone to account for our experimental results (see the SI appendix for full details).

Hindered diffusion layer. In the following, we relax the second assumption concerning the mobility of the ions. We then build a simple analytical model considering that ion mobility is not constant all over the film. For the sake of simplicity, we introduce a so-called hindered diffusion layer near the liquid-solid surface, where the mobility of counter-ions is fully inhibited. Such a molecular layer has been reported in other contexts, with the observation of decreased transport properties under confinement (23, 39, 54–59), or of an ice-like structure (41, 42, 60) in the vicinity of silica.

By assuming the ion motion is totally inhibited in a hindered diffusion layer of thickness δ next to the solid interface (see Fig. 3A), the electrophoretic velocity along the surface reads (i) $v(z) = \mu_+ \Delta V/\ell$ for $z < h - \delta$, with l the distance between the electrodes and μ_+ the ionic mobility of protons, (ii) $v = 0$ for $h - \delta \leq z \leq h$ in the hindered diffusion layer. Recalling that in our present case, the electro-osmotic contribution is negligible, the conductance then reads:

$$G = \frac{L}{\ell} 2\varepsilon k_B T \mu_+ K \tan\left[K(h-\delta)\right]. \qquad [2]$$

where K^{-1} is a characteristic length satisfying $Kh\tan(Kh) = 2\pi\ell_B h|\sigma|/e$ (see SI appendix for details). Note that when the hindered diffusion layer δ is small compared to the film thickness and in our conditions (see SI for details), this expression can be reduced to $G \simeq G_s \times (1 - \delta/h)$, with G_s the expected surface conductance for an homogeneous film without any hindered diffusion layer. For a constant surface charge, G_s is expected to be independent of the film thickness, and a plateau should be reached where a surface conductance is recovered (8, 11, 13). This is indeed the behavior we recover for large h.

Discussion

Fig. 3C shows the comparison between experimental data and the hindered diffusion description as given by Eq. (2). Overall this simple model captures well all the features of our experiments using the surface charge σ (assumed fixed) and the hindered layer thickness δ as free parameters. Values obtained for different substrates and for the loading/unloading branches are summarized in Table. 1.

First, the hindered diffusion layer thickness δ is found to be 0.31 ± 0.04 nm for all the data set, which is comparable to the size of one single water molecule and in good agreement with experiments reporting a structured stagnant layer of water adsorbed at an oxide interface. In the literature, the thickness of this layer however varies (from one to three molecular layers) with the type of properties that is considered (41, 42, 61). On a dynamical point of view, such stagnant layers have been observed experimentally when looking directly at hydrodynamic boundary conditions, with a fixed thickness of one molecular layer (62, 63). Second, the surface charge density σ is found to be around $-20\,\mu$C/m^2. In absolute value, it appears to be lower than measurements in the vicinity of silica in macroscopic systems (64). However, when considering charge regulation mechanism as discussed below, this value is in good agreement with expected ionization rate in such confined conditions (64).

Despite the good agreement between the model and the experiments, several hypotheses can be discussed. Concerning transport properties, we account for confinement and in particular friction at the water/silica interface by introducing the hindered diffusion layer, a first step towards more complex mobility profiles for the ions due to the presence of the surface. We also assume that the water-vapor interface is frictionless, which seems reasonable if the amount of adsorbed impurities is low (65).

Concerning our modeling of the ion distribution in the film (PB formalism), we have assumed that the dielectric permittivity of water was not modified by the confinement. Recent work suggests a decrease of the normal permittivity due to confinement (22, 24). Taking this effect into account, using $\varepsilon_r \simeq 2.1$, does not significantly modify the results (see SI appendix). For example, the surface charge extracted from the experimental data for the unloading cycle at $T_b = 6.01 \pm 0.02$ °C is shifted from 16.37 µC m^{-2} to 16.42 µC m^{-2} (the dashed green curve in Fig. 3C), a difference of one order of magnitude below the error bar of the measurements.

In addition, we note that to tune the relative humidity, we vary the temperature of the substrate. If we consider film thicknesses above 0.3 nm, the temperature variation is of around 15 °C, more precisely between $T = 6.0$ °C to $T = 20$ °C for case I, and $T = 15.9$ °C to $T = 30$ °C for case II. This could affect also our results as proton mobility has been shown to be dictated by a Grotthus mechanism and to increase with temperature, with a change of more than 10 % for a 10 °C variation (66, 67). This effect could explain the discrepancy between measurements performed at the two different temperatures that we have considered, the coldest one (case I) resulting in a lower conductance. However, this effect cannot be at the origin of the conductance collapse at low humidity (low film thickness), because low humidity is obtained by increasing the temperature, which can only increase the proton mobility and hence the conductance.

We also considered the liquid/vapor interface to be neutral, which is somewhat controversial. Specific charge adsorption at the water/vapor interface has been attributed either to impurities (68), or to specific anion adsorption. However, impurities should be very scarce here under low pressure environment. Moreover, in this water condensed film, the amount of anions is limited to spontaneous water dissociation, leading to a maximum surface density (if all the ions adsorb at the free surface) of 10 nC m^{-2}, which is very small compared to the surface charge density at the silica surface.

As already mentioned, another important restriction concerns the fixed surface charge hypothesis. A more accurate

charge regulation mechanism can be considered instead (44). In the SI appendix, we investigate different possible charge regulation models; here we will only briefly discuss a so-called single pKa model. In short, the surface charge density is controlled by the fraction φ_i of ionized groups at the surface: $\sigma = -e\varphi_i/a^2$, with a the average distance between each silanol sites. The fraction φ_i can be related to the constant K_a of the silanol dissociation reaction, and to the local proton concentration $c_+(z=h)$ at the surface (determined from the PB equation):

$$K_a = \frac{[SiO^-]\ c_+(z=h)}{[SiOH]} = \frac{\varphi_i}{1-\varphi_i}\, c_+(z=h). \qquad [3]$$

The surface charge density and surface potential can then be obtained by combining Eq. (3) and the electrostatic boundary condition. None of the charge regulation mechanisms that we have tested can properly account for experimental results, and in all cases a further hindered diffusion description is needed for protons mobility (see SI appendix). Within this hindered diffusion framework, both fixed charge and charge regulation perform well. Assuming a typical silanol mean distance of $a = 0.47\,\text{nm}$ (69), the corresponding surface charge can be estimated through the ionization fraction and the reaction constant as $\text{pKa} = 8.37 \pm 0.11$, in good agreement with the literature where a value of $\text{pKa} \simeq 9$ has been reported (47).

Finally, we used here a simple Gouy-Chapman model for the ions distribution near the substrate, neglecting the possible presence of a so-called Stern layer (70), in which the potential drops. It was experimentally shown that the magnitude of this layer is directly linked to the radius of adsorbed counter ions at the interface (71, 72). In our case, the amount of counter ions (here small protons) is limited and neglecting this contribution seems reasonable.

A natural extension would be to go beyond standard PB framework, to account for correlations and molecular steric repulsion (44, 48). But these two effects appear negligible in our situation. Indeed, a typical surface charge density, $-20\,\mu\text{C/m}^2$, results into sparse adsorption sites on the silica surface, with a mean distance d_i of 89 nm between each other. Then, the so-called plasma parameter, ℓ_B/d_i (49, 73, 74), which determines if correlations are important, is far smaller than one, meaning that correlations can be safely neglected. Note that extreme confinement can extend the range of electrostatic interactions and hence favor correlations (6); however, even considering the more stringent criterion imposed by the confinement, the mean inter-ionic distance d_i is large enough so that correlations can be neglected. Likewise steric effects are also negligible because d_i is by two orders of magnitude larger than the ion size, even considering the ion hydration shell (75, 76).

As a conclusion, we have presented a new approach towards exploring ionic transport in regimes of ultimate – molecular – confinement. Based on the spontaneous condensation of a liquid film atop a fully wettable substrate, our method allows us to continuously tune the liquid film thickness from 0.3 to 2 nm in an ultra-clean environment. For the largest film thicknesses $h \geq 1.2\,\text{nm}$, our conductance measurements on silica substrates recover the well-established surface conductivity regime (11, 13), whereas a strong departure is evidenced when reaching molecular confinement, which shows a non-linearly fading conductance. Strikingly, this effect can still be captured within a continuum description, provided that variations of the ion mobility in a monolayer of ions close to the wall, where protons motion is fully inhibited, are accounted for. These results are in contradiction with the existence of a highly conductive Stern layer in the vicinity of substrates (77, 78), or with observations of mobility enhancement in ultra-confinement (8, 14, 15, 79) in the vicinity of specific surfaces where the origin of charges is different. But they support well recent results in 2D water confined in graphene slits, that suggest that proton mobility is reduced by a factor of 20 (26) or, more generally, the existence of a stagnant hydrodynamic layer at the molecular scale in the vicinity of surfaces as observed for alkanes (62, 80) or water (54, 81). How phoretic and pressure driven transport are coupled in this molecular layer near an oxide surface remains an open question. Further studies could consider other types of liquids or substrates, such as van der Waals materials to test how the so-called Grotthus transport mechanism (57) is modified in ultra-confinement, for example. Finally, investigating the full film structure and its dynamical fluctuations in these regimes of ultraconfinement would be required to show the limits of continuous modelling.

Materials and Methods

Electrode Fabrication And Preparation. Commercially available silica substrates were used (WWD4 0525 250X 1618 S301, MicroChemicals). The SiO_2 layer was thermally grown on Si wafer by the dry/wet/dry way, with a thickness of 300 nm to minimize the current leakage. The Si bulk of the wafer is undoped. The roughness of the silica surface was characterized by an atomic force microscope (AFM, Asylum Research, MFP3D), and quantified by both the rms value (random mean square) and the profile height deviations from the mean line Ra, defined as $Ra = \frac{1}{L}\int_0^L |z(x)|\,dx$, with $z(x)$ the difference of altitude from the mean value. We fabricated the platinum electrodes following standard lithography methods as briefly detailed below (see SI appendix for additional elements). To efficiently detect the current in the liquid film, the electrode was designed in an interlaced comb-shaped geometry so that its total length went up to 1.49 m on a 300 mm^2 area. The width of the electrode beam and the spacing between each electrode branch is of the same size, 100 µm. The deposition pattern was achieved thanks to photolithography of a 1.5 µm photosensitive resin 409 type AZ5214 and lift-off. A first binding 10 nm-thick Titanium layer was first deposited, followed by the Platinum deposition. For this, we used an electron gun evaporator from Alliance Concept (model EVA300). The total deposited thickness is checked by profilometry (Dektak 150 model, from Bruker) and found to be 30 nm ±1 nm.

To build the electrical connection for the current detection, two circuit pin sites were stuck to the electrode by a silver conductive paint (RS 186-3600, RS PRO) and epoxy adhesive (EA 9492, Henkel) that are inert to the electrode cleaning. Each time prior to experiments, electrode was cleaned in the clean room according to the following protocol: the electrode was wiped multiple times with clean room tissues, respectively soaked with distilled water, ethanol and acetone, to remove visible surface contaminants; then it was placed into ethanol ultrasonic cleaning bath (Elma S100H, Elmasonic) to remove organic chemical groups for 5 minutes; after the ultrasonic bathing, it was dried with compressed air and further placed into oxygen plasma cleaner (PDC-002, Harrick Plasma) under high power for 3 minutes to further remove surface foreign chemical groups and enhance the surface wettability. Once the electrode was out of plasma cleaner, it was conserved into a petri dish and would be instantaneously brought to the vacuum chamber for conductivity measurements.

Experimental Control And Data Acquisition. The thickness of the liquid film was tuned by changing relative humidity in contact with the electrode SiO_2 interface. To achieve this purpose, the electrode

was placed on a thermal stage (Mk2000, Instec) of high precision $\pm 0.001\,^{\circ}\mathrm{C}$ so that the saturated vapor pressure at the SiO_2 interface could be controlled by setting the stage temperature. To keep physico-chemical properties of the SiO_2 interface during measurements, for example to avoid the airborne contamination, the electrode was placed inside a vacuum chamber (TS102V-F2, Instec) that was depressurized by a scroll vacuum pump (XDS10, Edwards). To stabilize the vapor pressure present on the electrode, the vacuum chamber was further connected to a vapor source filled with distilled water (18.2 $M\Omega{\cdot}cm$, PURELAB flex, ELGA) whose temperature was strictly set by a thermal bath (200F, Julabo) at 6 or $15.8\,^{\circ}\mathrm{C}$. This temperature was lower than the ambient temperature so that the system was free of condensation on all tube walls. Thus the vapor pressure, P, obeys the Clausius–Clapeyron relation under thermally quasi-equilibrium state and is computed thanks to the the IAPWS formulation 1995 (82). The whole system's leakage rate was $1.5\,\mathrm{Pa/\,min}$. To eliminate the accumulating effect of leakage and minimize the surface aging due to contamination, the vacuum pump continued to be rolling during conductance measurements and the suction flow rate inside the vacuum chamber was set at a small value by a metering valve (NY-2M-K6, Swagelok) with an opening of $5\,\mu\mathrm{m}$ to limit temperature variations in the liquid film. During the experiments, the vapor pressure inside the vacuum chamber was detected by a capacitance gauge (CMR362, Pfeiffer Vacuum).

To measure the liquid film thickness as a function of relative humidity, a spectro-ellipsometer (J.A Woolam M-2000) was adapted to the same vacuum apparatus. The beam angle was set at 70° and the reflected signal was measured for various wavelengths ranging from 300 to 1000 nm. The polarized incident light was reflected by the substrate, and its intensity and polarization were detected and analyzed. The Si wafer with a 10 nm to 20 nm-thick SiO_2 layer on top was cleaned with the same cleaning protocol as described for the electrode. The reason for using a thinner SiO_2 layer is that the condensed liquid film thickness, typically of 1 nm, is two orders smaller than a 300 nm SiO_2 layer such that the thickness measurement of the liquid film is drowned into the noise according to the three layers model to extract water film thickness. The thin SiO_2 layer was deposited by Plasma Enhanced Chemical Vapor Deposition technique at *INL* on a p-type (Boron) Si wafer (WSD2 0279 250B 1314 SNN1 MicroChemicals). As it consists in amorph SiO_2 layers and only water/SiO_2 interface is considered, it is reasonable to assume that thick thermally grown SiO_2 layer and thin deposited SiO_2 layer are equivalent. Moreover, it was shown that varying the SiO_2 thickness did not change our experimental results. One-minute ellipsometer scanning for liquid film thickness and 3 minutes waiting gap before the next run were maintained all throughout and three-times run for each case was performed to reduce the statistical errors and ensure measurement reproducibility.

For the conductance measurements, a home-made I/V converter was developed to convert small currents to detectable voltages. The voltage sent out to the electrode and that received after the I/V converter were obtained through a digital-analogic card (NI USB-6216, National Instruments) controlled remotely by a python script. The applied voltage to the electrode was a sinusoidal wave of 10 Hz with the magnitude of 1 V. The choice of a periodic wave is to avoid the accumulation of ions and possible electrode aging or polarization in our system. Voltage of 1 V is below the hydrolysis voltage so that no hydrolysis is expected during measurements. The sampling rate of the acquisition was set to 2000 Hz. The complex conductance was then calculated based on the applied voltage and measured current. Each measurement lasted 30 s and was repeated three times to minimize statistical errors. Recovery time was kept at least 3 minutes before the next measurement when the experimental condition changed so that the system had enough time to reach its equilibrium. All the data were analyzed with python codes.

More details on data analysis and apparatus details can be found in SI appendix.

ACKNOWLEDGMENTS. The authors thank Benjamin Fornacciari for deposition of SiO_2 layer on Si wafer via plasma enhanced chemical vapor deposition, Agnès Piednoir for AFM measurements, Gilles Simon for building mechanical set-ups, nanoptec center for access ellipsometric measurements. This project was funded by the ANR project Soft Nanoflu (ANR-20-CE09-0025-03), and the IDEXLYON project from Lyon University in the program PIA (ANR-16-IDEX-0005).

References.

1. DA Doyle, et al., The structure of the potassium channel: molecular basis of k+ conduction and selectivity. *science* **280**, 69–77 (1998).
2. A Siria, ML Bocquet, L Bocquet, New avenues for the large-scale harvesting of blue energy. *Nat. Rev. Chem.* **1**, 1–10 (2017).
3. W Guan, R Fan, MA Reed, Field-effect reconfigurable nanofluidic ionic diodes. *Nat. communications* **2**, 1–8 (2011).
4. JJ Kasianowicz, E Brandin, D Branton, DW Deamer, Characterization of individual polynucleotide molecules using a membrane channel. *Proc. Natl. Acad. Sci.* **93**, 13770–13773 (1996).
5. Y Xu, Nanofluidics: a new arena for materials science. *Adv. Mater.* **30**, 1702419 (2018).
6. N Kavokine, RR Netz, L Bocquet, Fluids at the nanoscale: From continuum to subcontinuum transport. *Annu. Rev. Fluid Mech.* **53**, 377–410 (2021).
7. T Mouterde, et al., Molecular streaming and its voltage control in ångström-scale channels. *Nature* **567**, 87–90 (2019).
8. A Esfandiar, et al., Size effect in ion transport through angstrom-scale slits. *Science* **358**, 511–513 (2017).
9. E Secchi, et al., Massive radius-dependent flow slippage in carbon nanotubes. *Nature* **537**, 210–213 (2016).
10. K Falk, B Coasne, R Pellenq, FJ Ulm, L Bocquet, Subcontinuum mass transport of condensed hydrocarbons in nanoporous media. *Nat. communications* **6**, 1–7 (2015).
11. A Siria, et al., Giant osmotic energy conversion measured in a single transmembrane boron nitride nanotube. *Nature* **494**, 455–458 (2013).
12. FH van der Heyden, DJ Bonthuis, D Stein, C Meyer, C Dekker, Power generation by pressure-driven transport of ions in nanofluidic channels. *Nano letters* **7**, 1022–1025 (2007).
13. D Stein, M Kruithof, C Dekker, Surface-charge-governed ion transport in nanofluidic channels. *Phys. Rev. Lett.* **93**, 035901 (2004).
14. E Secchi, A Niguès, L Jubin, A Siria, L Bocquet, Scaling behavior for ionic transport and its fluctuations in individual carbon nanotubes. *Phys. review letters* **116**, 154501 (2016).
15. H Liu, et al., Translocation of single-stranded dna through single-walled carbon nanotubes. *Science* **327**, 64–67 (2010).
16. S Balme, et al., Ionic transport through sub-10 nm diameter hydrophobic high-aspect ratio nanopores: experiment, theory and simulation. *Sci. reports* **5**, 1–14 (2015).
17. VM Aguilella, C Verdiá-Báguena, A Alcaraz, Lipid charge regulation of non-specific biological ion channels. *Phys. Chem. Chem. Phys.* **16**, 3881–3893 (2014).
18. BW Ninham, VA Parsegian, Electrostatic potential between surfaces bearing ionizable groups in ionic equilibrium with physiologic saline solution. *J. theoretical biology* **31**, 405–428 (1971).
19. OI Vinogradova, EF Silkina, ES Asmolov, Enhanced transport of ions by tuning surface properties of the nanochannel. *Phys. Rev. E* **104**, 035107 (2021).
20. G Gonella, et al., Water at charged interfaces. *Nat. Rev. Chem.* **5**, 466–485 (2021).
21. N Kavokine, ML Bocquet, L Bocquet, Fluctuation-induced quantum friction in nanoscale water flows. *Nature* **602**, 84–90 (2022).
22. L Fumagalli, et al., Anomalously low dielectric constant of confined water. *Science* **360**, 1339–1342 (2018).
23. U Raviv, S Perkin, P Laurat, J Klein, Fluidity of water confined down to subnanometer films. *Langmuir* **20**, 5322–5332 (2004).
24. DJ Bonthuis, RR Netz, Unraveling the combined effects of dielectric and viscosity profiles on surface capacitance, electro-osmotic mobility, and electric surface conductivity. *Langmuir* **28**, 16049–16059 (2012).
25. J Feng, et al., Observation of ionic coulomb blockade in nanopores. *Nat. materials* **15**, 850–855 (2016).
26. K Gopinadhan, et al., Complete steric exclusion of ions and proton transport through confined monolayer water. *Science* **363**, 145–148 (2019).
27. X Jiang, et al., Nonlinear electrohydrodynamic ion transport in graphene nanopores. *Sci. advances* **8**, eabj2510 (2022).
28. B Radha, et al., Molecular transport through capillaries made with atomic-scale precision. *Nature* **538**, 222–225 (2016).
29. T Emmerich, et al., Enhanced nanofluidic transport in activated carbon nanoconduits. *Nat. Mater.* **21**, 696–702 (2022).
30. Y You, et al., Angstrofluidics: walking to the limit. *Annu. Rev. Mater. Res.* **52**, 189–218 (2022).
31. A Horner, P Pohl, Single-file transport of water through membrane channels. *Faraday discussions* **209**, 9–33 (2018).
32. U Vermesh, et al., Fast nonlinear ion transport via field-induced hydrodynamic slip in sub-20-nm hydrophilic nanofluidic transistors. *Nano letters* **9**, 1315–1319 (2009).
33. C Duan, A Majumdar, Anomalous ion transport in 2-nm hydrophilic nanochannels. *Nat. nanotechnology* **5**, 848–852 (2010).
34. PG De Gennes, Wetting: statics and dynamics. *Rev. modern physics* **57**, 827 (1985).
35. D Bonn, J Eggers, J Indekeu, J Meunier, E Rolley, Wetting and spreading. *Rev. modern physics* **81**, 739 (2009).
36. L Joly, C Ybert, E Trizac, L Bocquet, Hydrodynamics within the electric double layer on slipping surfaces. *Phys. review letters* **93**, 257805 (2004).
37. O Bonhomme, O Liot, AL Biance, L Bocquet, Soft nanofluidic transport in a soap film. *Phys. review letters* **110**, 054502 (2013).
38. Y Ma, et al., Dimension-reconfigurable bubble film nanochannel for wetting based sensing. *Nat. communications* **11**, 1–11 (2020).
39. R Sarfati, DK Schwartz, Temporally anticorrelated subdiffusion in water nanofilms on silica suggests near-surface viscoelasticity. *ACS nano* **14**, 3041–3047 (2020).
40. A Verdaguer, G Sacha, H Bluhm, M Salmeron, Molecular structure of water at interfaces: Wetting at the nanometer scale. *Chem. reviews* **106**, 1478–1510 (2006).

41. A Verdaguer, et al., Growth and structure of water on sio2 films on si investigated by kelvin probe microscopy and in situ x-ray spectroscopies. *Langmuir* **23**, 9699–9703 (2007).
42. DB Asay, SH Kim, Evolution of the adsorbed water layer structure on silicon oxide at room temperature. *The J. Phys. Chem. B* **109**, 16760–16763 (2005).
43. A Alam, M Howlader, M Deen, The effects of oxygen plasma and humidity on surface roughness, water contact angle and hardness of silicon, silicon dioxide and glass. *J. Micromechanics Microengineering* **24**, 035010 (2014).
44. JN Israelachvili, *Intermolecular and surface forces*. (Academic press), (2011).
45. J Visser, On hamaker constants: A comparison between hamaker constants and lifshitz-van der waals constants. *Adv. Colloid Interface Sci.* **3**, 331–363 (1972).
46. O Vincent, B Marguet, AD Stroock, Imbibition triggered by capillary condensation in nanopores. *Langmuir* **33**, 1655–1661 (2017).
47. AM Darlington, JM Gibbs-Davis, Bimodal or Trimodal? The Influence of Starting pH on Site Identity and Distribution at the Low Salt Aqueous/Silica Interface. *J. Phys. Chem. C* **119**, 16560–16567 (2015).
48. D Andelman, Electrostatic Properties of Membranes: The Poisson-Boltzmann Theory in *Handbook of Biological Physics*. (Elsevier) Vol. 1, (1995).
49. C Herrero, L Joly, Poisson-boltzmann formulary. *arXiv preprint arXiv:2105.00720* (2021).
50. L Bocquet, E Charlaix, Nanofluidics, from bulk to interfaces. *Chem. Soc. Rev.* **39**, 1073–1095 (2010).
51. H Daiguji, P Yang, A Majumdar, Ion transport in nanofluidic channels. *Nano letters* **4**, 137–142 (2004).
52. S Pennathur, JG Santiago, Electrokinetic transport in nanochannels. 1. theory. *Anal. chemistry* **77**, 6772–6781 (2005).
53. DG Haywood, ZD Harms, SC Jacobson, Electroosmotic flow in nanofluidic channels. *Anal. chemistry* **86**, 11174–11180 (2014).
54. TD Li, J Gao, R Szoszkiewicz, U Landman, E Riedo, Structured and viscous water in subnanometer gaps. *Phys. Rev. B* **75**, 115415 (2007).
55. Y Gao, et al., Anomalous solid-like necking of confined water outflow in hydrophobic nanopores. *Matter* **5**, 266–280 (2022).
56. WH Zhao, et al., Highly confined water: Two-dimensional ice, amorphous ice, and clathrate hydrates. *Accounts chemical research* **47**, 2505–2513 (2014).
57. J Comtet, et al., Direct observation of water-mediated single-proton transport between hbn surface defects. *Nat. Nanotechnol.* **15**, 598–604 (2020).
58. O Vincent, A Szenicer, AD Stroock, Capillarity-driven flows at the continuum limit. *Soft Matter* **12**, 6656–6661 (2016).
59. S Gruener, T Hofmann, D Wallacher, AV Kityk, P Huber, Capillary rise of water in hydrophilic nanopores. *Phys. Rev. E* **79**, 067301 (2009).
60. G Algara-Siller, et al., Square ice in graphene nanocapillaries. *Nature* **519**, 443–445 (2015).
61. PK Gupta, M Meuwly, Dynamics and vibrational spectroscopy of water at hydroxylated silica surfaces. *Faraday discussions* **167**, 329–346 (2013).
62. J Georges, S Millot, J Loubet, A Tonck, Drainage of thin liquid films between relatively smooth surfaces. *The J. chemical physics* **98**, 7345–7360 (1993).
63. M Cieplak, J Koplik, JR Banavar, Boundary conditions at a fluid-solid interface. *Phys. Rev. Lett.* **86**, 803 (2001).
64. SH Behrens, DG Grier, The charge of glass and silica surfaces. *The J. Chem. Phys.* **115**, 6716–6721 (2001).
65. L Joly, F Detcheverry, AL Biance, Anomalous ζ potential in foam films. *Phys. review letters* **113**, 088301 (2014).
66. B Cornish, R Speedy, Proton conductivity in supercooled aqueous hydrochloric acid solutions. *The J. Phys. Chem.* **88**, 1888–1892 (1984).
67. A Kornyshev, A Kuznetsov, E Spohr, J Ulstrup, Kinetics of proton transport in water (2003).
68. K Roger, B Cabane, Why are hydrophobic/water interfaces negatively charged? *Angewandte Chemie Int. Ed.* **51**, 5625–5628 (2012).
69. L Zhuravlev, The surface chemistry of amorphous silica. zhuravlev model. *Colloids Surfaces A: Physicochem. Eng. Aspects* **173**, 1–38 (2000).
70. J Lyklema, *Fundamentals of Interface and Colloid Science: Vol. II - Solid/Liquid Interfaces*. (Academic press), (1995).
71. MA Brown, et al., Determination of surface potential and electrical double-layer structure at the aqueous electrolyte-nanoparticle interface. *Phys. Rev. X* **6**, 011007 (2016).
72. I Siretanu, et al., Direct observation of ionic structure at solid-liquid interfaces: a deep look into the stern layer. *Sci. reports* **4**, 1–7 (2014).
73. RR Netz, H Orland, Beyond poisson-boltzmann: Fluctuation effects and correlation functions. *The Eur. Phys. J. E* **1**, 203–214 (2000).
74. Y Levin, Electrostatic correlations: from plasma to biology. *Reports on progress physics* **65**, 1577 (2002).
75. H Daiguji, Ion transport in nanofluidic channels. *Chem. Soc. Rev.* **39**, 901–911 (2010).
76. MS Kilic, MZ Bazant, A Ajdari, Steric effects in the dynamics of electrolytes at large applied voltages. i. double-layer charging. *Phys. review E* **75**, 021502 (2007).
77. C Zukoski IV, D Saville, The interpretation of electrokinetic measurements using a dynamic model of the stern layer: I. the dynamic model. *J. colloid interface science* **114**, 32–44 (1986).
78. C Zukoski IV, D Saville, The interpretation of electrokinetic measurements using a dynamic model of the stern layer: Ii. comparisons between theory and experiment. *J. colloid interface science* **114**, 45–53 (1986).
79. P Pang, J He, JH Park, PS Krstić, S Lindsay, Origin of giant ionic currents in carbon nanotube channels. *ACS nano* **5**, 7277–7283 (2011).
80. DY Chan, R Horn, The drainage of thin liquid films between solid surfaces. *The J. chemical physics* **83**, 5311–5324 (1985).
81. U Raviv, J Klein, Fluidity of bound hydration layers. *Science* **297**, 1540–1543 (2002).
82. W Wagner, A Pruß, The IAPWS formulation 1995 for the thermodynamic properties of ordinary water substance for general and scientific use. *J. Phys. Chem. Ref. Data* **31**, 387–535 (2002).